MODIFICATIONS TO THE HOUGHTON XRD

By

Sarah Olandt

A thesis submitted in partial fulfillment of the requirements for the degree of

Bachelor of Science

Houghton College

Dec 20, 2019

Signature of Author……..
Department of Physics
Dec 20, 2019

……..
Dr. Brandon Hoffman
Professor of Physics
Research Supervisor

……..
Dr. Mark Yuly
Professor of Physics

MODIFICATIONS TO THE HOUGHTON XRD

By

Sarah Olandt

Submitted to the Department of Physics
on Dec 20, 2019 in partial fulfillment of the
requirement for the degree of
Bachelor of Science

Abstract

Modifications have been made to the Houghton College X-ray Diffractometer (XRD) which will be used for analysis of thin films. The Bragg-Brentano theta 2-theta XRD contains a Phillips-Norelco x-ray source powered by a 40 kV power supply. A Vernier student radiation monitor is mounted to a Lin Engineering 101411 stepper motor to collect data that is analyzed using LoggerPro software. Adjustments have been made to the LabVIEW program used to control the stepper motors for the radiation monitor and the thin film sample in order to maintain consistency and accuracy as they rotate along a semi-circular path. Safety modifications have also been completed, including shielding and interlocks for the apparatus to protect the surrounding room as x-rays are directed towards the sample.

Thesis Supervisor: Dr. Brandon Hoffman
Title: Professor of Physics

TABLE OF CONTENTS

TABLE OF FIGURES

Chapter 1

INTRODUCTION

1.1. History

1.1.1. Discovery of X-Rays

Wilhelm C. Röntgen discovered a new kind of electromagnetic radiation [1] while studying high-voltage electrical discharges through dilute gases in a Crook's tube on November 8th, 1895. Röntgen published this discovery [2] on December 28, 1895 describing what he then called x-rays which originated from within the tube and created a bright fluorescence on a shield of black paper that did not allow ultra-violet light to pass through. Röntgen also detailed several experiments that he had conducted on these rays, which are called Röntgen rays, and his conclusions. Röntgen found that materials such as paper and tinfoil have little to no effect on the passing of the rays, but other materials, such as lead, have the ability to block the rays. In the course of his experiments on these materials, Röntgen placed a hand by the shield and was able to see the bones clearly as shown in Figure 1.

Figure 1. X-ray image of Röntgen's wife's hand. This image was obtained by placing the hand in between the source of the x-rays and photographic paper. Image taken from Ref [2].

Röntgen's original publication on x-rays included many preliminary observations and in 1901 earned him the very first Nobel Prize in physics. Among Röntgen's early observations was the nature of these rays to travel in a straight line without regular reflection or refraction [2]. Röntgen also noted that x-rays were very different from any known ultra-violet rays at the time of their discovery. Due to this, little was known or understood about their nature.

Competing theories about x-rays arose after their discovery, reflecting the common theories of light at the time. Röntgen believed that x-rays were electromagnetic radiation [2-3] propagating through the ether, just as light was believed to do. Others however, believed that x-rays were a flux of electrically charged particles [4-6]. The proponents of each theory continued to experiment with and observe x-rays in order to better understand their nature, eventually disproving Röntgen's ether theory. These experiments also gave increasing insight into the characteristics of x-rays.

A major breakthrough based on the 1893 Helmholtz dispersion theory [7-8] came in 1897, which suggested that electromagnetic waves of short wavelengths would not be reflected or refracted, fitting the original observations of x-rays. Observations of x-rays put them in this category and thus the electromagnetic theory of x-rays was developed. From this theory, Arnold Sommerfeld was able to determine that the wavelength of an x-ray [3,9] was on the order of 10^{-11} m. While this development took a while to confirm experimentally, in 1911 Charles Barkla [7,10] published his findings that two types of characteristic x-radiation result from heavy elements, which helped to further the electromagnetic theory of x-rays. As physicists continued to develop their understanding of the nature of x-rays and to experimentally determine their wavelength, Sommerfeld and others turned their attention towards diffraction.

1.1.2. X-ray Diffraction

Max Laue began working for Sommerfeld in 1909 and by 1911 had developed a new theory for diffraction, something that had been of interest to those experimenting with x-rays since Röntgen's original discovery. While many experimentalists had been using crystals as targets for x-rays and experimenting with sending x-rays through slits for diffraction purposes [2,11-15], there had not yet been any diffraction behavior recorded. The wavelengths of x-

rays were unknown to experimentalists at the time, which suggests that experimental arrangements used dimensions too large for the detection of diffraction in x-rays. While some research was conducted with this in mind by Walter and Pohl [15], they were unable to see any effects of diffraction. They were however able to estimate the wavelength of x-rays. After consulting with P. P. Ewald whose work focused on the lattice structure of crystals, and taking into account the estimates of x-ray wavelength [7], Laue hypothesized that crystal lattices could act as diffraction gratings for x-rays.

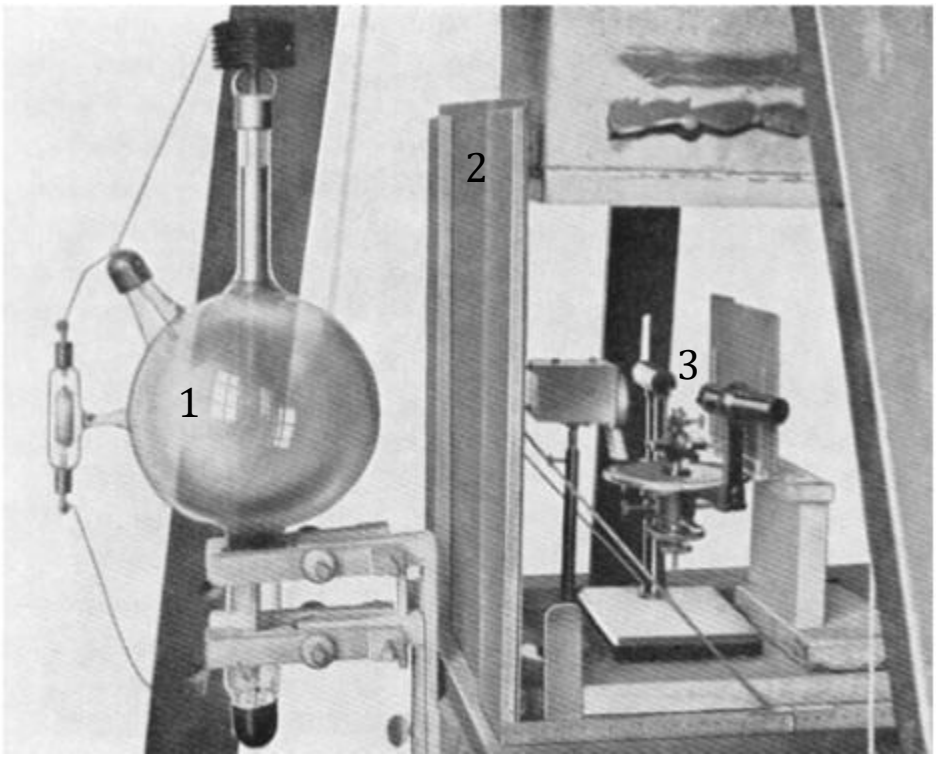

Figure 2. Experimental apparatus used by Friedrich and Knipping in the discovery of x-ray diffraction patterns using crystal lattices. X-rays are produced in the glass bulb (1) and travel through a small hole in the metal shielding (2) which directs them through the crystal (3) to a photographic plate. Figure taken from Ref. [7].

This idea was tested by Walter Friedrich [16] and Paul Knipping in 1912. Friedrich and Knipping's experiment directed a narrow beam of x-rays from an anticathode to pass through a copper sulfate crystal onto a photographic plate as shown in Figure 2. This produced the first diffraction pattern seen from x-rays which appeared on the photographic plate as dark spots arranged in a regular pattern as shown in Figure 3. From this, Laue was

able to conclude that the x-ray diffraction pattern was a result of the crystal structure, which supported Laue's original ideas about x-ray diffraction by crystals.

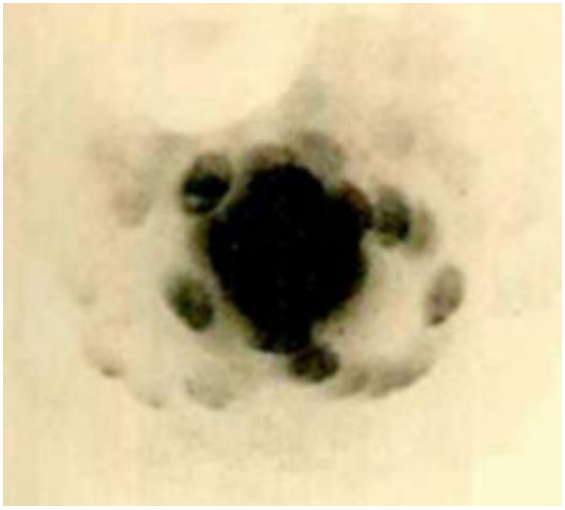

Figure 3. First x-ray diffraction pattern obtained by Friedrich and Knipping in 1912 using a copper sulfate crystal to diffract the x-ray beam before hitting the photographic plate. This image shows an ordered pattern of dark spots from the diffracted rays. Figure taken from Ref. [7].

Further experiments using different materials with crystal structure yielded similar results, and experimental techniques were improved to continue this line of research, resulting in more defined and clear diffraction patterns. In 1914, Laue was awarded [3] the Nobel Prize in physics for the discovery of x-ray diffraction in crystals.

1.1.3. Bragg's Research

Since x-ray diffraction had been of interest to many physicists even before Laue was awarded the Nobel Prize for his discovery, the field continued to receive much attention. Two notable contributors to the field of x-ray diffraction are William Henry and William Lawrence Bragg who explored the phenomena of diffraction to better understand the mechanisms causing it.

While Laue was able to achieve x-ray diffraction based on his ideas about the crystal acting as a diffraction grating, there was still a great deficit of understanding as to how x-ray diffraction actually worked. W.L. Bragg believed that an explanation [17] for x-ray diffraction was possible by assuming that the incident radiation came in pulses with a continuous spectrum of wavelengths, spanning a large range. Bragg believed that some wavelengths

within the spectrum would have greater intensity and the energy of other wavelengths would fall off from this maximum. This meant that the waves reflecting off of a set of planes in the crystal would neutralize each other if came at an angle too low and if they came at an angle too large, the pulses would be too far apart to create the intensity for spots.

Shortly after Bragg's publication suggesting that a continuous spectrum of x-ray wavelengths was responsible for the diffraction patterns seen from crystals, W.H. Bragg and W.L. Bragg published their findings [18-19] that x-rays of the same wavelengths hitting off of parallel planes within a crystal under certain conditions create constructive interference. Their work related the angle at which x-rays hit the crystal, the wavelength of the x-rays, the spacing between planes in the crystal to the spots of maximum intensity seen in diffraction experiments. This has become known as Bragg's Law and earned the father-son pair the Nobel Prize in 1915.

Another [19] of the Braggs' contributions to the growing field of x-ray diffraction was a new method to create and study diffractions. The Braggs modified a spectrometer to use as their tool of investigation. An ionization chamber was able to rotate about a revolving table that held the crystal and the x-ray source was blocked by a lead shield with a small hole to allow only a very narrow beam of x-rays to pass through to the sample. This arrangement, shown in Figure 4, allowed the Bragg's to conduct the necessary experiments to confirm that Bragg's law worked in crystals. In addition to Laue's photography method and the later methods of powder diffraction, this has become an important tool in fields relying on x-ray diffraction analysis, including crystallography and thin film research.

1.2. Thin Film Research and X-ray Analysis

Thin metal films are used in several industries, including microelectronics and other electronics such as memory devices. The mechanical and electrical properties of the materials that make up these films are determined in part by their microstructures; therefore, it is important to understand the material's microstructure in order to predict and better understand and control film properties. Research has been ongoing in this field and previous research [20] by Houghton College, in collaboration with Cornell University, has used X-ray Diffraction analysis to study texture transformations in thin Ag films.

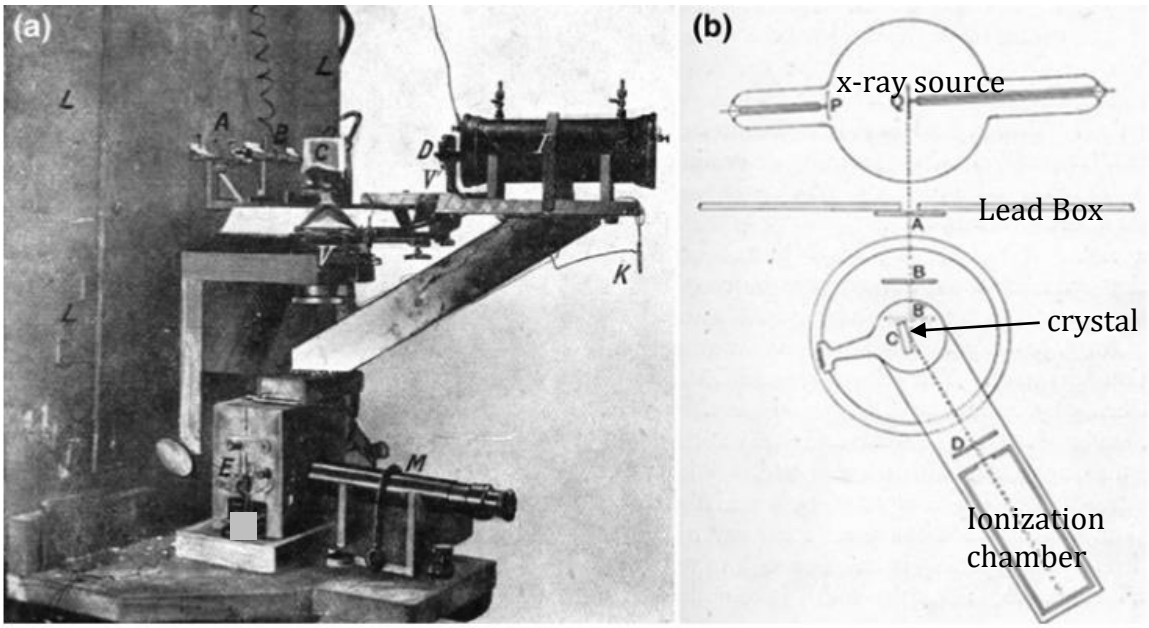

L	lead box	*E*	Electroscope
A B D	slits	*V*	Vernier of crystal table
C	crystal	*V'*	Vernier of ionization chamber
I	Ionization chamber	*M*	Microscope

Figure 4. Bragg's spectrometer (a) and schematic drawing (b). The x-ray source is contained in a lead box and x-rays pass through slits A and B allowing only a narrow beam to pass through to the crystal C. X-rays reflect off of the crystal and are directed through slit D into an ionization chamber. The crystal and ionization chamber are both able to rotate around the vertical same axis. Images taken from Ref. [7].

1.2.1. Thin films

Thin films are characterized by a thickness typically on the order of nanometers and several orders of magnitude smaller than both the width and length of the films. The structure of atoms in these materials can be one of several lattice structures. Each material has a specific lattice structure determined by the element or elements that make up that material. One such structure that can be exhibited by thin film materials is face centered cubic (FCC), which will be used here for example purposes.

Lattice structures are three dimensional arrangements of repeated unit cells of atoms and are named for the shape of that unit cell. Cubic structures, as the name suggests, are structures whose unit cells are cubes and these cubes are repeated in three dimensions to form the lattice. This means that the atoms forming the unit cell can be visualized as being

placed at different points on a cube. FCC is one type of cubic structure in which atoms are located at each of the eight corners of the cube and at the center of each of the six faces of the cube, as shown in Figure 5. Some materials commonly studied in thin film research that exhibit FCC structure include Gold (Au), Silver (Ag), Copper (Cu), and Platinum (Pt).

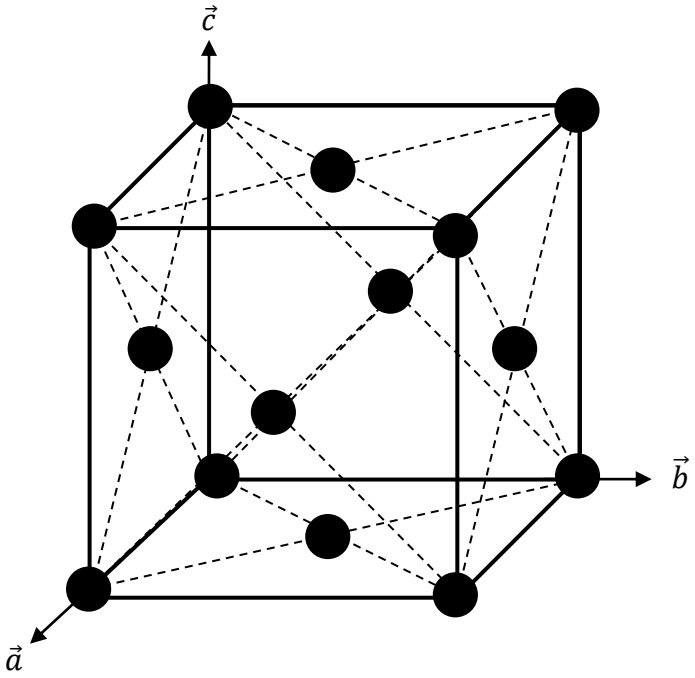

Figure 5. Diagram of a face centered cubic arrangement of atoms in a crystal. Atoms are arranged at all corners of the cube as well as at the center of each cube face. This lattice structure was determined by Bragg to be responsible for the first x-ray diffraction experiments observed and is most common in materials studied at Houghton College.

1.2.1.1. Planes and Miller Indices

If the atomic arrangement in a lattice is viewed from different angles, it can be seen that the atoms form several different planes. Each plane intersects the a, b, and c axes at different places. Figure 6 shows how the planes in an FCC crystal intersect the cube of atoms in different ways, thereby including different atoms and creating a unique arrangement of atoms for various planes. These planes become more clear when looking at the larger three-dimensional structure formed from several unit cells. In the larger structure, the spacing between adjacent planes depends on the type of plane. For example, the spacing between

two (100) planes, as show in Figure 6, is different than the spacing between two (111) planes, also shown in Figure 6.

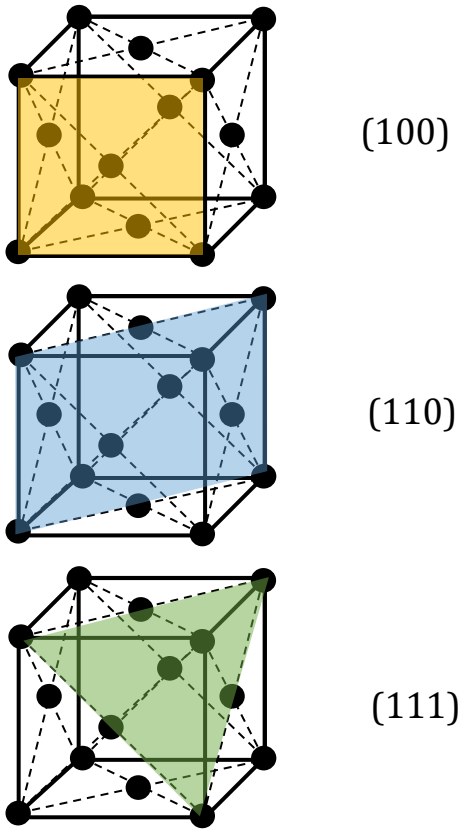

Figure 6. Planes in FCC crystal structure. Each plane through the cubic structure exhibits its own arrangement of atoms and corresponds to a different orientation. The top image represents a (100) plane, the middle image a (110) plane, and the bottom image a (111) plane. The spacing between planes in a sample is different for each type of plane shown above (and others that exist with a crystal lattice).

The specific configuration of atoms that constitute any given plane in a lattice is described by a set of Miller indices which include one index for every dimension in the crystal structure. The FCC structure contains three dimensions in a Cartesian coordinate system: a, b, and c. The corresponding Miller indices used to convey the orientation in FCC crystals are (*hkl*), where each refers to one of the three dimensions. Miller indices are determined by the reciprocal of the fractional intercepts that the given plane makes with the crystallographic axis; the axes in FCC being a, b, and c. The reciprocals are then converted into the smallest whole number ratios. For example, the (110) plane shown in the middle image of Figure 6

has an a-intercept of 1, a b-intercept of 1, and the plane is parallel to the c-axis so the c-intercept is ∞. Taking the reciprocal of these intercepts gives $^1/_1$ for a, $^1/_1$ for b, and $^1/_\infty$ for c; this translates to the (110) orientation.

The Miller indices used to describe a plane also correspond to the normal vector for the plane; the normal vector being $\vec{n} = h\hat{a} + l\hat{b} + k\hat{c}$. From this, the unit vector of the normal direction for any plane can be obtained:

$$\hat{n} = \frac{h\hat{a} + k\hat{b} + l\hat{c}}{\sqrt{h^2 + k^2 + l^2}}. \quad (1)$$

where h, k, and l are the Miller indices and $\hat{a}$, $\hat{b}$, and $\hat{c}$ are the crystallographic axes, normalized to the length of that edge of the unit cell.

Within the unit cell, there can be several planes that have the same configuration of atoms within them but are facing different directions and have different Miller indices.. One example of this is the planes that are formed by each face of the unit cell, as shown in the top image of Figure 6. These planes are described with different Miller indices such as (100), (001), and (010). Due to the symmetry of the unit cell, however, if the cube is rotated 90 degrees in any direction it remains identical. This means that each of these planes is also identical. Therefore, in this paper no distinction will be made between planes whose Miller indices contain the same set of three indices, i.e. the face planes in FCC will all be referred to as (100).

1.2.1.2. Grains and Film Textures

When several unit cells are lined up together in three dimensions, they form a crystal. In thin films, several crystals can exist that are not all aligned in the same direction, this creates a polycrystalline film. Groups of atoms or unit cells that do line up, creating a periodic atomic arrangement, also form grains. The planes formed by the atoms in any given grain will all be parallel with normal vectors pointed in the same direction. The orientation of a grain is defined by which plane is parallel to the substrate surface in that grain. Grain boundaries occur when the periodicity of the atoms is broken which occurs when crystals are misaligned.

The texture of a film describes the orientations of the grains within the sample. If the grains are randomly orientated, then there is no distinct texture to the film. If the grains exhibit some preferred orientation, then the sample is said to have a texture. The texture for a film whose orientation is not random can be strong, moderate, or weak depending on what percentage of the grains in the sample have the preferred orientation. For example, if a sample has a preferred (111) orientation and a large percent of grains in that sample are oriented in the (111) direction, the sample would have a strong (111) texture.

1.2.2. XRD Analysis in Thin Films

There are several different microscopy techniques available for determining the texture of a thin film. X-ray diffraction (XRD) analysis is one of the lesser time-consuming analysis methods and may not require the same level of operator training. XRD analysis is useful in gaining insight into the texture and makeup of a thin film.

X-ray diffraction measures the intensity of x-rays diffracted from a sample at different angles. Different orientations of atoms will diffract x-rays at different angles. This method provides an overall view of the orientations of the crystal within a sample, and their relative intensities. XRD analysis can also be used to measure grain size, but it does not give an image to reference as methods such as SEM and TEM do.

1.2.2.1. Texture studies using XRD

The texture of thin films is important because texture determines mechanical properties of the film; if the texture could be controlled, films could be created with whatever properties are desired. However, while the crystallographic theory behind texture has been well developed, much is still unknown regarding what affects a film's texture and how texture changes over time. Research regarding texture change has been ongoing [20-23] across several avenues. It is commonly cited in these studies that existing theories attribute texture change to the movement of grain boundaries, but this work strives to understand the driving forces behind the transformation in more detail.

One study by Sonnweber-Ribic et al. [21] looked at several Cu films of different thicknesses after a 2-hour annealing period. XRD analysis was used to measure the macrotexture of the

samples while electron backscatter diffraction (EBSD) was used to look the distribution of local orientations. Comparison of EBSD and XRD scans revealed that the texture of the samples changed from a large number of (111) oriented grains in thinner films to mostly (100) oriented grains in thicker films. When the driving forces of surface/interface energy minimization and strain energy minimization were considered, the texture transformation was found to relate to the crossover in which driving force was stronger. However, the results of driving force analysis were unable to explain the broad transition in texture across different thicknesses.

A later study by Sonnweber-Ribic et al. [22] also aimed to improve understanding of microstructure and texture changes. This study looked at four thicknesses of Cu films annealed at different temperatures. Periodic EBSD scans were performed and XRD scans were conducted after the total anneal time was reached. This study again found a decrease in (111) oriented grains with increasing film thickness and revealed abnormal growth of (100) oriented grains. Higher (100) fractions were found in the final samples of films annealed at hotter temperatures and thicker films. XRD scans were used to determine stress values and dislocation densities for the samples which revealed that the driving forces previously explored (surface/interface energy minimization and strain energy minimization) were not adequate to cause the (100) oriented preferential growth. A mechanism involving the linear increase in dislocation energy with film thickness was proposed to remedy this. This mechanism, however, remained to be explained.

Another study, by Baker et. al. [20], explored the effects of film thickness and the addition of a Ti adhesion layer in Ag films. As in the studies described above, XRD scans of these films also showed that thicker films transform to (100) orientation while thinner films retain a (111) orientation after annealing. However, this study found no evidence that stress or interface energy controlled the transformation as was suggested in the studies by Sonnweber-Ribic et al. [21-22]. This study [20] also concludes that a driving force for texture transformation is associated with defects or dislocations in the interior of the grains, posing the question of how a reduction in this energy leads to transformation.

A later study by Ellis et al. [23] explored the driving force of defect energy in Ag films proposed by Baker et al. [20]. This study [23] again found a texture transformation in all films, using XRD, that went from a strong (111) texture to a strong (100) texture and concluded that strain energy minimization was not responsible for the transformation. It was calculated that a reduction in energy occurring when new defect-free grains grow to replace existing grains containing defects could provide the necessary driving force when the defects being eliminated were nanotwins. However, it was also noted that this driving force only accounts for a small amount of the driving force for grain growth and suggests that a more complicated model of driving forces may be needed.

These studies have shown that the driving forces behind texture transformation are not only impacted by grain boundary movements. The evidence suggests that defects in the grains likely act as a driving force for the transformation as well. However, the specifics of this driving force have not yet been determined and further research is necessary to gain a more complete understanding.

1.2.3. XRD Research at Houghton

Current thin film research at Houghton College is investigating the effects of different elements of film deposition on the deformities present in as-deposited films and the overall texture transformations in Ag films. This research strives to complete the information obtained in previous research regarding defect energy as a driving force for texture transformation.

To determine the texture transformation of these films, XRD analysis is being used to compare initial and final textures. As-deposited XRD scans of the Ag films provide the relative amounts of different orientations present in the films. This provides the initial, or as-deposited texture of the film. XRD scans of the same sample after periods of annealing provide the relative amounts of the orientations in the film after annealing. By comparing the relative amounts before and after annealing, texture change can be observed.

To date, data collection for this research has been conducted in collaboration with Dr. Shefford Baker at Cornell University. All XRD scans have been obtained using the facilities at

the Cornell Center for Materials Research. This has imposed limitations to the duration of time during which data collection can be completed and has restricted the volume of data with which this research is conducted.

1.2.3.1. The Houghton XRD

A project has been ongoing to develop a functioning Bragg-Brentano theta 2-theta XRD at Houghton College to aid in current research, allowing for data collection to continue year-round, resulting in a greater volume of data for the research to move forward. The basic elements of this machine have been installed, including an x-ray source with connections for a power source and water-cooling system, a high voltage power supply, a radiation monitor, and motors to facilitate scans of varying angles. Several safety features however, require completion. Likewise, improvements to the resolution capabilities of the machine and the reproducibility of the motors are necessary before the Houghton XRD can be put into use full-time for research purposes.

Chapter 2

THEORY

X-ray diffractometers, or XRDs, use x-rays to analyze samples. The analysis process requires the production of x-rays, which occurs in an x-ray source where electrons are accelerated towards a target material. The x-rays created through this process are then incident on a sample, reflect off of the sample, and then interact with each other. These interactions result in different intensities for the reflect rays which is what the XRD ultimately measures.

2.1. X-Ray Production

X-rays are a form of electromagnetic radiation that results when accelerated electrons are incident on a target. When the electrons hit the target, they are either stopped, or they knock off electrons from the atoms of the target material and electrons within the atom fill the hole that is left. X-rays are the result of the energy released in these scenarios. They have a wavelength between 0.01 nm and 10 nm and travel in straight lines unless they encounter objects in their paths.

2.1.1. X-Ray Tube

One of the most common methods of x-ray production is the use of an x-ray tube like the one shown in Figure 7. The vacuum of this tube contains two electrodes connected by a filament that acts as the cathode. The cathode and the circuit that powers it, as shown in Figure 8, are floating at a high negative voltage and the electrodes that are attached to a filament are supplied with a potential difference. A battery is used to supply this potential difference. This causes electrons from the filament to accelerate towards the anode material, which is connected to ground. As the high-energy electrons hit the metal in the anode, x-rays are produced.

2.1.2. Bremsstrahlung x-rays

The high energy electrons coming off of the cathode lose energy when they interact with the anode material. Because interactions with atoms in the target material only result in the loss of some energy from the accelerated electrons, it can take several interactions for the

electrons to be completely stopped. As the electrons interact with the target atoms, they are slowed down and the energy they lose as they slow down produces radiation of different energies and therefore different wavelengths.

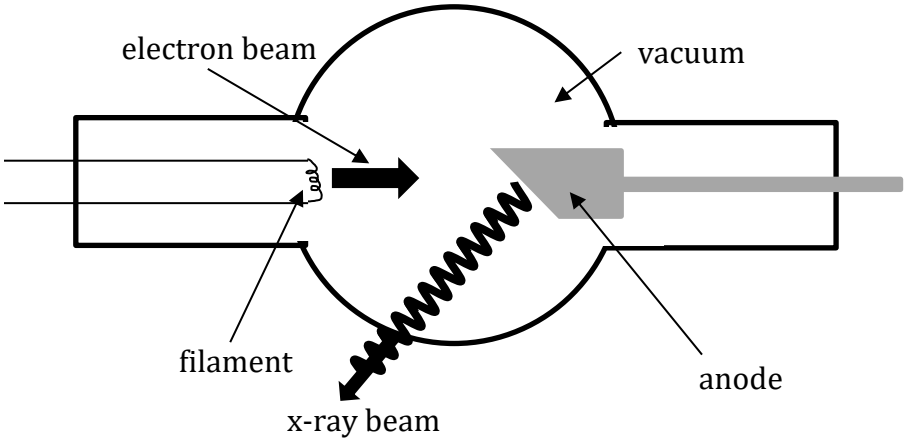

Figure 7. Diagram of an x-ray tube. Electrons accelerate off the filament and travel towards the anode. The electron interactions with the anode are responsible for the creation of x-rays.

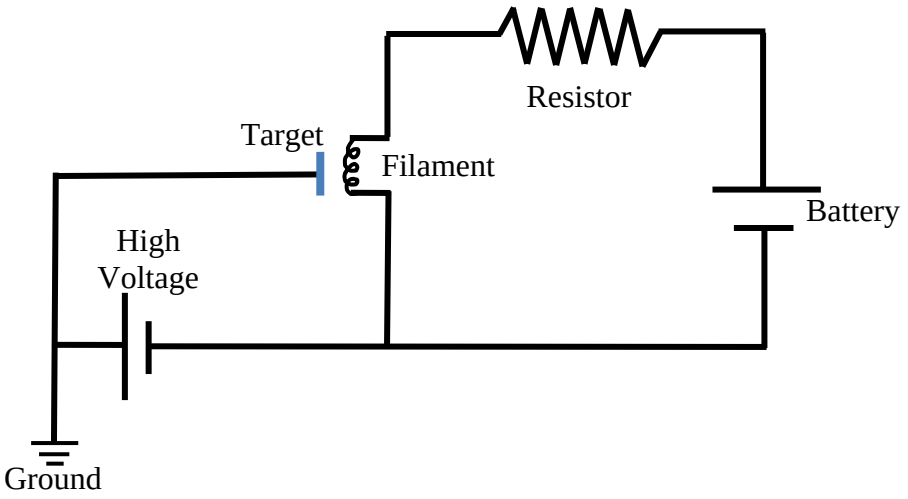

Figure 8. General circuit diagram for powering an x-ray source. The circuit powering the filament is connected to a high voltage power source to float the filament at the high voltage while the target is connected to ground. A battery powers the filament, which causes electrons to come off the filament and move towards the grounded target.

The radiation produced lacks discrete values of energy because different electrons can lose all different amounts of energy as they lose velocity. This produces a continuous band of energies as seen in Figure 9, which corresponds to the x-rays that are produced. Because this spectrum of x-rays results from the slowing down and stopping of electrons, it is referred to as Bremsstrahlung x-rays, coming from the German word for "braking radiation". Bremsstrahlung x-rays were reported in 1912 by Sommerfeld [24].

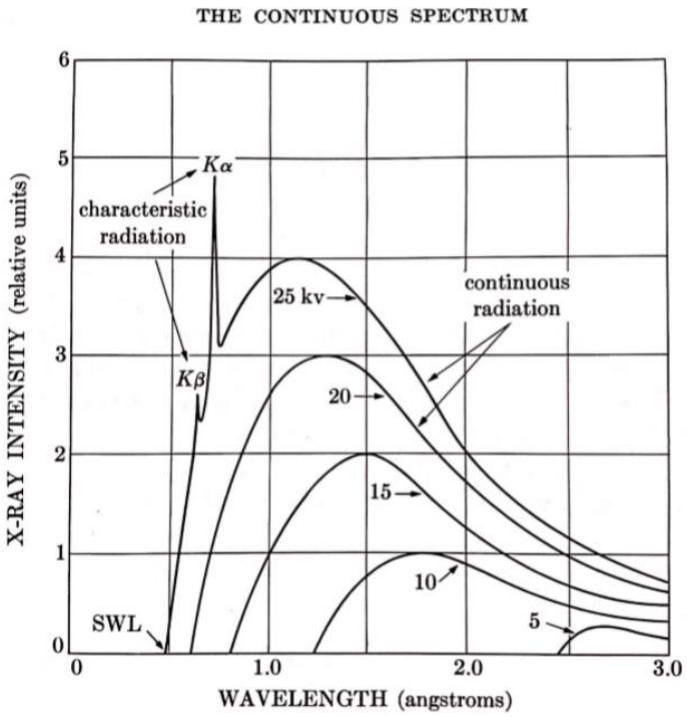

Figure 9. X-ray spectrum of molybdenum. The wavelength of x-rays produced by the stopping of electrons is plotted on the x-axis while the measured intensity of the x-rays is measured on the y-axis. Each line represents a different voltage applied to the x-ray tube. The two peaks in intensity represent characteristic x-rays while the curves show the Bremsstrahlung x-rays. Figure taken from Ref. [25].

2.1.3. Characteristic x-rays

Characteristic x-rays were first reported in 1911 by Barkla [10]. As electrons are accelerated from the cathode towards the anode, they can also interact with the orbital electrons in the anode material. High energy electrons from the cathode can knock out inner shell electrons from the anode material. Electrons in higher energy level shells then drop into the level with the hole left by the ejected electron. As this transition occurs, a photon is also released from

the target atom. The photon contains an equivalent amount of energy as is associated with the electron's transition between energy levels.

The discrete energy values associated with these photons are responsible for the discrete energy of characteristic x-rays which can be predicted by the material used in the anode. Depending on what shell the ejected electron leaves a hole in and what shell the transitioning electron comes out of, the resulting x-rays will have different amounts of radiation. For x-ray diffraction, the electron transition from the n=2 to the n=1 shell, which produces K-alpha x-rays as seen in Figure 9, is most commonly relied upon.

2.1.4. Byproducts

The production of x-rays from the cathode/anode interaction creates the undesirable biproduct of heat which results from the energy of the accelerated electrons that is not converted into either Bremsstrahlung or characteristic x-rays. To maintain a safe temperature for operation, the x-ray tube must be cooled. X-rays tubes are often designed so that a continuous stream of water can flow through a hollow section of the anode. The excess heat is transferred from the anode material to the water, which is constantly being replaced, allowing the x-ray tube to function safely for extended periods of time.

2.2. X-Ray Diffraction

Once x-rays are created, they will travel in a straight line, unless they interact with a material whose properties cause a change. Almost all materials absorb x-rays to some extent and almost all materials also reflect x-rays. Dense materials such as lead absorb a lot of the x-rays while other materials such as plastic absorb very little of the x-rays. Materials made from crystals also diffract x-rays, changing the path of the incident rays. When x-rays are reflected, the path alteration is determined by the material and by the nature of x-rays as electromagnetic radiation. The reflected x-rays also interact with each other in ways that give information about the material the reflected off of.

2.2.1. Wave Interference

X-rays are understood to be transverse sine waves modeled as

$$\psi = Ae^{i\varphi} = Ae^{i(\vec{\kappa}\cdot\vec{x}-\omega t)} \quad (2)$$

where A is the amplitude, φ is the phase of the wave, $\vec{\kappa}$ is the wave vector, $\vec{x}$ is the wave position in space, ω is the angular frequency, and t is the time. It is assumed that all x-rays coming from the source have the same amplitude.

When transverse waves interact with each other, they create interference that can either be constructive or destructive. This occurs in x-ray diffraction when the x-rays reflect off of the atomic layers in a sample as depicted in Figure 10.

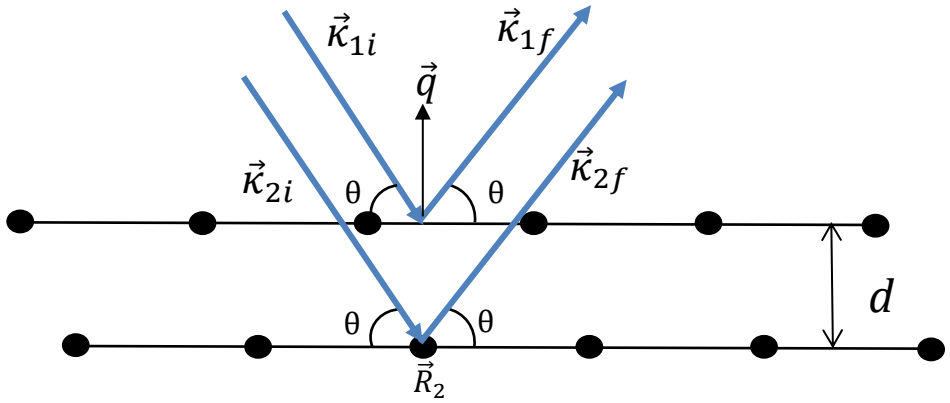

Figure 10. Diagram of x-ray diffraction on sample planes with incident and outgoing vectors labelled. X-rays that reflect off different planar layers are denoted with different numeric subscripts.

When incident x-rays travel through a sample, different x-rays reflect off of different planes, as seen in Figure 10, the x-rays that reflect off of the second layer, travel a further difference. The position of the atom in the second plane is denoted $\vec{R}_2$, and is equal to d in the above figure. This means that the phase difference between incoming rays hitting the first plane and the second plane is $\vec{\kappa}_i \cdot \vec{R}_2$, and the phase difference between the outgoing x-rays is $\vec{\kappa}_f \cdot \vec{R}_2$. In the wavefunction, this looks like

$$\psi_{2f} = f_j e^{i(0+\vec{\kappa}_i \cdot \vec{R}_2 - \vec{\kappa}_f \cdot \vec{R}_2)} \tag{3}$$

where f_j includes the atomic form factor which will be discussed in the Section 2.3.2. It is important to note that the amplitude that is seen in Equation (2) becomes f_j in Equation (3) because this equals the amplitude of the incoming wave multiplied by the form factor.

We can define $\vec{q} \equiv \vec{\kappa}_f - \vec{\kappa}_i$, which is the scattering vector. When the incoming and outgoing rays make the same angle with the planes of the sample, the scattering vector is normal to the plane. Thus, the wavefunction then becomes

$$\psi_{2f} = f_j e^{-i(\vec{q}\cdot\overrightarrow{R_2})} \tag{4}$$

and consequently, for the x-rays hitting the first plane of the sample, the wavefunction of the deflecting x-ray is

$$\psi_{1f} = f_j e^{-i(\vec{q}\cdot\overrightarrow{R_1})}. \tag{5}$$

For the first x-ray however, $\vec{R}_1$ is equal to zero because it is the origin of the coordinate system used to define the atoms. This means that $\vec{q} \cdot \vec{R}_1 = 0$ as well, and that the wave hitting the top layer of the sample, $\overrightarrow{k_1}$, does not travel any extra distance with respect to itself. Because $\vec{R}_j$ can be applied to any x-ray that is incident on the sample, it can be said in general that the wavefunction for any one outgoing x-ray is

$$\psi_{jf} = f_j e^{-i(\vec{q}\cdot\vec{R}_j)}. \tag{6}$$

In order to find the wavefunction to describe all of the outgoing x-rays in XRD, one must sum each individual wavefunction to get

$$\psi_f = \sum_{j=1}^{N} f_j e^{-i(\vec{q}\cdot\vec{R}_j)} \tag{7}$$

where N is the number of atomic layers in the sample.

Equation (7) gives the equation for the interference of x-rays reflected off the sample. If the individual x-rays interfere constructively, the resulting wave will have a larger amplitude than the incident waves. This is what creates larger intensities of x-rays as detected in x-ray diffractometry. The geometry of the sample determines when this constructive interference occurs.

2.2.2. Bragg's Law

When the understanding of x-rays was still in its infancy, the father-son pair, W.H. Bragg and W.L. Bragg [18] explored the mechanisms that created the constructive interference of x-rays when reflected off of crystal samples. They were able to formulate a mathematical model to predict which angles of incidence for incoming x-rays will lead to constructive interference in the outgoing diffracted rays that produce the intensity seen in diffraction patterns.

Bragg's equation can be derived from the equation for interference, Equation (7). The atomic form factor can be pulled out of the sum because it is equal for atoms that are the same and the atoms in a sample are all identical. The wavefunction then becomes

$$\psi_f = f \sum_{j=1}^{N} e^{-i(\vec{q}\cdot\vec{R}_j)}. \tag{8}$$

For the sake of simplicity, looking at waves reflecting from the first and second planes, the summation yields the following wave equation:

$$\psi_f = f(\psi_1 + \psi_2) = f\left(e^{-i(\vec{q}\cdot\vec{R}_1)} + e^{-i(\vec{q}\cdot\vec{R}_2)}\right) \tag{9}$$

where $\vec{R}_1 = 0$, as stated above, making $\vec{R}_1 = d$ and $q = 2\kappa \sin\theta$, and $\kappa \equiv 2\pi/\lambda$. Because q points normal to the plane and $\vec{R}$ is the position of the atom on the first plane, they point antiparallel, thus:

$$\vec{q}\cdot\vec{R} = -2d\left(\frac{2\pi}{\lambda}\right)\sin\theta. \tag{10}$$

The wavefunction in Equation (9) therefore becomes

$$\psi_f = f(1 + \psi_2) = f\left(1 + e^{-i\left(-2d\left(\frac{2\pi}{\lambda}\right)\sin\theta\right)}\right). \tag{11}$$

Maximum intensity of the wave occurs when $\psi_2 = 1$, this happens when

$$-2d\left(\frac{2\pi}{\lambda}\right)\sin\theta = n2\pi. \tag{12}$$

This model is most commonly known as Bragg's Law:

$$n\lambda = 2d \sin\theta \tag{13}$$

where d is the interplanar spacing in the crystal lattice of the material, λ is the wavelength of the incident x-rays, n is an integer corresponding to the interference node, and θ is the angle of incidence between the incoming x-rays and the sample surface as seen in Figure 11. Equation (13) requires that, for a maximum constructive interference, the path wavelength difference must be a multiple of the wavelength.

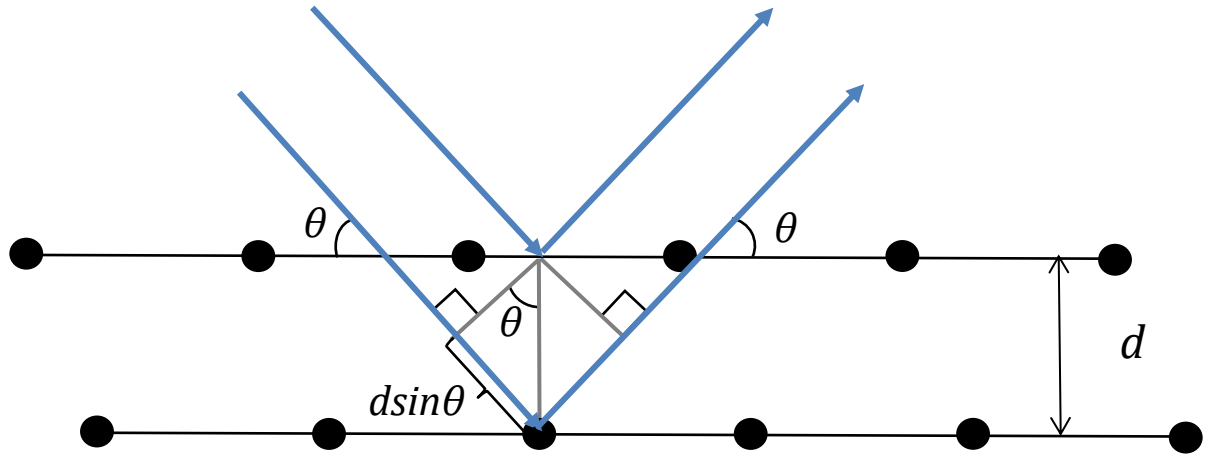

Figure 11. Diagram of Bragg's Law. Incident x-rays make an angle θ with the plane of the sample surface and are deflected by different planes within the sample. The resulting outgoing x-rays travel different lengths which are related by 2dsinθ.

The diffracted x-rays leaving the sample all have the same wavelength because they result from the same incoming x-rays. This means that maximum constructive interference between two outgoing x-rays occurs when the waves are separated by an integer multiple of the wavelength. Bragg's Law utilizes this assessment and gives the incident angle that creates the maximum constructive interference. As the incident angle θ changes, the combined outgoing waves intensity will transition gradually between constructive and destructive interference when modeled for only the first two planes. As more planes are considered, the transition will be more distinct since the range of angles that result in a final

wavefunction greater than zero approaches one single value as the number of planes goes to infinity.

2.3. Correction Factors

In XRD analysis, the diffracted x-rays depend on more than just the angle of incidence of the incoming x-rays. The intensity of diffracted x-rays at a given Bragg angle depends also on the amount of the crystals within the sample oriented so that the planar spacing corresponds to that specific Bragg angle. Due to this, XRD is often used to determine the percentage of a material that exhibits a specific orientation, but other factors that contribute to the intensity of the diffracted x-rays must be accounted for before this can be done.

2.3.1. Structure Factor

The structure factor is a correction made necessary by the fact that waves scattering from a surface will scatter to different positions. To begin understanding the structure factor, one must first look at the combined wave function described in Equation (8).

In this equation, $\vec{q}$ is the scattering vector, normal to the surface, as shown in the scattering diagram in Figure 10. As stated above, $q = 2\kappa \sin\theta$ which means that $\vec{q}$ can be written as

$$\vec{q} = 2\kappa \sin\theta \, \hat{n} \tag{14}$$

where the $\hat{n}$ gives the direction of $\vec{q}$ and can be written in terms of the Miller indices h, k, l and the unit vectors of the crystal lattice, given by Equation (1).

From Equations (14) and (1) we see that

$$\vec{q} = 2\kappa \sin\theta \frac{h\hat{a} + k\hat{b} + l\hat{c}}{\sqrt{h^2 + k^2 + l^2}}. \tag{15}$$

The position of an atom in terms of the unit vectors of the crystal lattice can be written as

$$\overrightarrow{R_j} = a(x_j\hat{a} + y_j\hat{b} + z_j\hat{c}) \tag{16}$$

where a is the lattice constant for the material of the sample and x_j, y_j, z_j are the distances of the atom in units of a. From this, the scattered phase, which depends on the scattering vector and the position of the atoms, becomes

$$\vec{q} \cdot \vec{R}_j = (2\kappa \sin\theta) a \left[\frac{hx_j + ky_j + lz_j}{\sqrt{h^2 + k^2 + l^2}} \right]. \tag{17}$$

For a crystal lattice structure, the geometric relationship between the planar spacing d and the lattice constant a is

$$d = \frac{a}{\sqrt{h^2 + k^2 + l^2}}. \tag{18}$$

Using Bragg's Law from Equation (13) and the geometric relationship from Equation (18), the scattered phase in Equation (17) simplifies to

$$\vec{q} \cdot \vec{R}_j = 2n\pi \left(hx_j + ky_j + lz_j \right). \tag{19}$$

Keeping in mind Equation (7), for $n = 1$, the scattered wavefunction can then be written

$$\psi_f = \left(\frac{N}{m} \right) \left[f_{2\theta} \sum_{j=1}^{m} e^{-i2\pi \left(hx_j + ky_j + lz_j \right)} \right] \tag{20}$$

where the atomic form factor is taken out of the sum and given the subscript 2θ because it depends on the scattering angle 2θ. Note that this summation is no longer over N atoms but only over the m atoms in the basis, which depends on the crystal structure, because all the cells contribute equally. Multiplying the structure factor by $\left(\frac{N}{m} \right)$ accounts for the entirety of the crystal. This summation in this wavefunction is defined as

$$F_{hkl} = \left[f_{2\theta} \sum_{j=1}^{m} e^{-i2\pi \left(hx_j + ky_j + lz_j \right)} \right] \tag{21}$$

where F_{hkl} is the structure factor.

The structure factor for the FCC crystal structure, where there are four atoms in the basis (one at the origin ((which is a corner)) and three face atoms), is

$$F_{hkl} = f_{2\theta}\left(e^{-i2\pi(0)} + e^{-i2\pi(h/2+k/2)} + e^{-i2\pi(h/2+l/2)} + e^{-i2\pi(k/2+l/2)}\right). \quad (22)$$

2.3.2. Atomic Form Factor

Another correction factor that arises in x-ray diffraction is the atomic scattering (or form) factor. This accounts for the scattering of x-rays by the electrons in the atoms of the sample. When the x-ray beam hits an atom, two types of scattering occur. Loosely bound electrons in the atom scatter part of the incident x-ray beam and the wavelength of the beam is increased with a dependence on scattering angle. This is incoherent scattering which produces a background intensity that varies with 2-theta. Tightly bound electrons in the atom can oscillate when the x-ray beam is incident on them and give off x-rays of the same wavelength. This is called coherent scattering which is necessary for diffraction.

The atomic form factor describes the efficiency or power of both coherent and incoherent scattering from a single atom and depends on the number of electrons and the Bragg angle; it gives the amplitude of the scattered waves as a function of the angle at which the x-rays scatter.

Unlike the structure factor which uses a summation to account for x-rays scattering off of atoms in different positions which are discrete and do not represent a continuous range, the atomic form factor must sum over a continuous region, the electron cloud. The sum seen in the above section therefore must become an integral over all space:

$$f'_{2\theta} = \int \rho e^{iq\cdot r} dV \quad (23)$$

where ρ is the position-dependent scattering density, r is the position, and V is the volume. Notice that this integral takes a similar form to the summation in Equation (7) for the structure factor.

Equation (23) is not easily solved. However, the atomic form factor may be approximated with the following sum of Gaussians:

$$f'_{2\theta} \approx \sum_{i=1}^{4} a_i e^{-b_i\left(\frac{q}{4\pi}\right)^2} + c = \sum_{i=1}^{4} a_i e^{-b_i\left(\frac{\sin\theta}{\lambda}\right)^2} + c \tag{24}$$

where the coefficients a_i, b_i, and c for several elemental materials can be found in reference tables. Values for the atomic form factor at different values of $\frac{\sin\theta}{\lambda}$ for various elements can be found in the International Tables of X-ray Crystallography [26].

2.3.3. Polarization Factor

The incident beam of x-rays used in x-ray diffraction is unpolarized and thereby creates the need for a polarization correction factor. This unpolarized ray can be broken up into two polarized rays whose electric field vectors are components of the electric field vector of the original x-ray beam as seen in Figure 12.

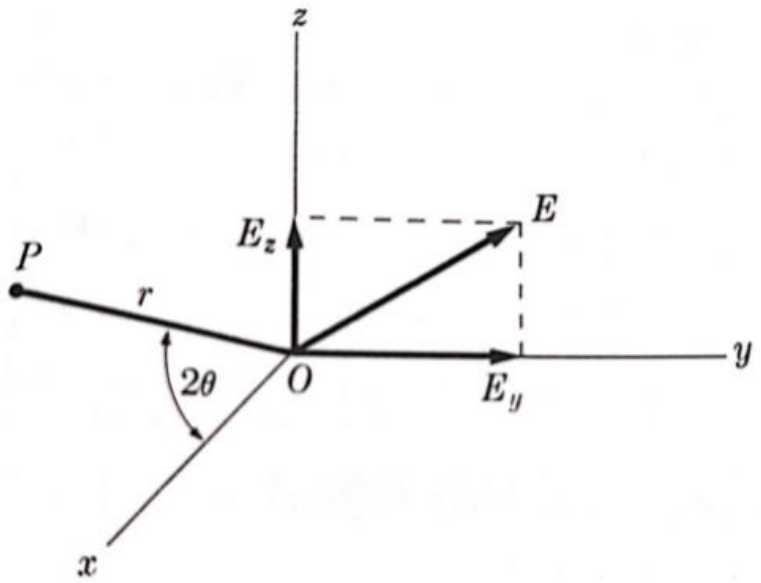

Figure 12. X-ray beam scattered by an electron. An incident beam travels in the positive x-direction and is incident upon an electron at the origin O. This results in a beam scattered to point P in the xz-plane and distance r from the electron. The electric field of the unpolarized incident beam is broken into y and z-components. The scattered beam lies in the xz-plane, making the angle 2θ with the x-axis. Figure taken from Ref. [25].

The polarization factor is determined by looking at an x-ray incident on a single electron. J.J. Thomson [6] determined the intensity of a beam of x-rays scattered by an electron of charge e and mass m to be

$$I = I_o \frac{e^4}{r^2 m^2 c^4} \sin^2 \alpha \tag{25}$$

where r is the distance between the scattered beam at point P and the electron, α is the angle between the direction of acceleration of the electron and the direction of the scattering beam, c is the velocity of light, and I_o is the intensity of the incident beam. Defining

$$K \equiv \frac{e^4}{m^2 c^4} \tag{26}$$

Equation (25) simplifies to

$$I = I_o \frac{K}{r^2} \sin^2 \alpha. \tag{27}$$

Looking to Figure 12, if a beam is traveling in the x-direction and is incident on an electron at the origin O, the intensity at a point P in the xz-plane can be determined. Notice that the scattering angle off of the x-axis to point P is equal to 2θ.

As mentioned above, the electric field vector of the unpolarized incident beam can be viewed as components:

$$E^2 = {E_y}^2 + {E_z}^2. \tag{28}$$

Because the incident beam is unpolarized, the direction of its total electric field will be random. Therefore, on average, the components E_y and E_z will be equal in magnitude and equal to ½ of the total electric field vector:

$${E_y}^2 = {E_z}^2 = \frac{1}{2} E^2. \tag{29}$$

The intensity of a wave is proportional to the square of its electric field because the electric field measures the amplitude of the wave and intensity is proportional to the amplitude squared. Therefore,

$$I_{0y} = I_{0z} = \frac{1}{2} I_0 \tag{30}$$

for the incident beam.

From Equation (27) it can be seen that the y-component of the incident beam will result in a scattered beam whose intensity in the y-direction at point P is given by

$$I_{Py} = I_{oy} \frac{K}{r^2} \tag{31}$$

because the angle between the y-component of the incident beam and the direction of the scattered beam is $\frac{\pi}{2}$ and $\sin^2\left(\frac{\pi}{2}\right) = 1$. The intensity of the scattered beam at point P in the z-direction is given by

$$I_{Pz} = I_{oz} \frac{K}{r^2} \cos^2 2\theta \tag{32}$$

because the angle between the direction of the scattering beam and the z-component of the incident beam is $(90° - 2\theta)$ and $\sin(90° - 2\theta) = \cos 2\theta$.

Adding Equations (31) and (32) to find the total intensity of the scattered beam yields

$$I = \frac{K}{r^2}\left(I_{0y} + I_{0z} \cos^2 2\theta\right). \tag{33}$$

Taking into consideration Equation (30), this simplifies to

$$I = \frac{K}{r^2}\left(\frac{I_0}{2} + \frac{I_0}{2} \cos^2 2\theta\right) = \frac{I_0}{2} \frac{K}{r^2} (1 + \cos^2 2\theta) \tag{34}$$

which gives rise to the polarization factor

$$I \propto (1 + \cos^2 2\theta) \tag{35}$$

when the constant terms are neglected, and only angular dependence is considered.

2.3.4. Lorentz Factor

During XRD scans of thin films, the amount of time that each orientation is position to the reflect x-rays at the Bragg condition is unequal [27]. Due to this, the intensity of the reflected x-rays from each orientation is proportional to the amount of time that an orientation is in the position to reflect the x-rays. This necessitates the Lorentz factor.

The conditions of Bragg's Law determine the scattering vector $\vec{q}_b$ that corresponds to constructive interference. This vector has a length equal to 2nπ, where n is an integer, as seen in Bragg's Law. The magnitudes of the incoming ($\vec{k}_i$) and outgoing ($\vec{k}_f$) wave numbers are also constant, as they are set by the x-ray source. Figure 13 shows how these facts can be related to geometrically express the limitations created. The dotted circle represents the possible values of $\vec{k}_f$ based on the position of $\vec{k}_i$ and the wave numbers.

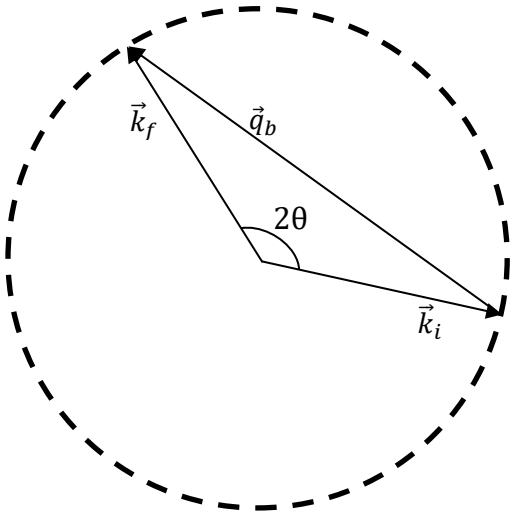

Figure 13. Diagram of scattering vector, initial wave number and final wave number. The circle indicates all the possible values of the final wave number $\vec{k}_f$ that satisfy the conditions for Bragg's Law. $\vec{k}_f$ and $\vec{k}_i$ have the length because they are determined by the x-ray source which is the same for all the x-rays.

For the symmetric theta-2theta arrangement of XRD scans, the scattering vector $\vec{q}_b$ is always oriented normal to the surface. As the sample is rotated with a constant angular velocity ω, the direction of the scattering vector will change. This can be viewed as rotating the scattering vector, rather than the sample, at constant angular velocity. As stated above, the conditions for Bragg's Law are met when the scattering vector is in the position shown in

Figure 13. However, real crystals can create interference in reflected x-rays when the angle of incidence of the x-ray beam differs from the Bragg angle by some small amount, that is to say, when the scattering vector is slightly off from the position shown in Figure 13. Due to this variation, the intensity of the scattered beam will depend on how long the scattering vectors is near the position required by Bragg's Law. This can be expressed as:

$$\int Id\theta \propto \frac{1}{\vec{v}_p \cdot \vec{k}_f} = \frac{1}{\omega q_b \cos(\varphi)} \propto \frac{1}{q_b \cos(\varphi)} \tag{36}$$

where $\vec{v}_p$ is the velocity of the point to which the scattering vector reaches and φ is the angle between $\vec{v}_p$ and $\vec{k}_f$. These relationships can be seen in Figure 14.

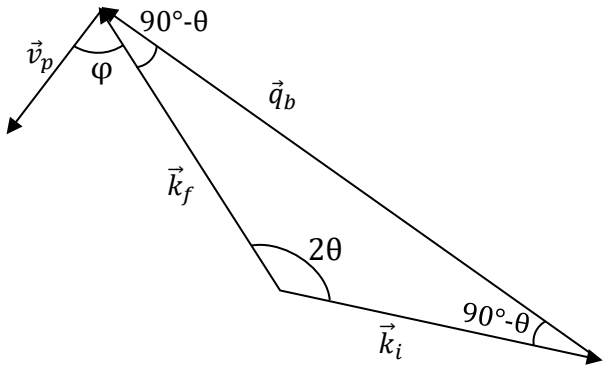

Figure 14. Diagram of relationships in the Lorentz correction factor. $\vec{v}_p$ indicates the velocity at which the point at the end of the scattering vector $\vec{q}_b$ moves. The velocity vector is perpendicular to the scattering vector.

From Figure 14 it can be seen that $\varphi = \theta$. The law of sines for this situation gives

$$\frac{sin(2\theta)}{q_b} = \frac{sin(90-\theta)}{k} = \frac{\cos\theta}{k}. \tag{37}$$

From this information, it can be seen that

$$q_b \cos\varphi = q_b \cos\theta = k\cos(2\theta). \tag{38}$$

Using Equation (38) to simplify Equation (36), the Lorentz correction factor L becomes:

$$\int I d\theta \propto L = \frac{1}{\sin(2\theta)}. \tag{39}$$

2.3.5. Attenuation Factor

As x-rays are incident on the sample, some intensity will be absorbed into the sample, giving rise to the attenuation factor. The decrease in intensity of x-rays as they travel through matter [6] is described by

$$I = I_0 e^{-\mu l} \tag{40}$$

where μ is the attenuation coefficient specific to the x-ray energy and the matter through which it travels, and *l* is the distance that the x-ray travels through the material.

In XRD analysis, x-rays are incident on the sample as some angle θ and penetrate the sample to a depth of z and then exit the sample again at the same angle θ as shown in Figure 15

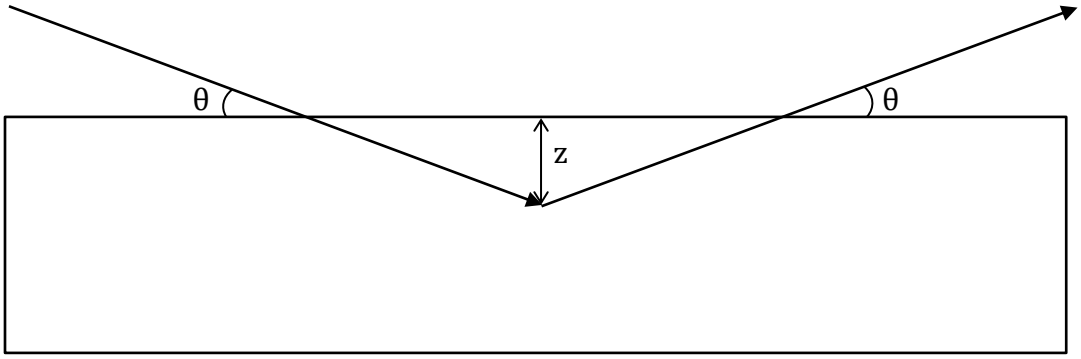

Figure 15. Diagram of depth penetration of x-rays in samples. X-rays enter the sample at the incident angle θ, travel a depth z into the sample, and exit the sample at and angle equal to the angle of incidence θ.

The geometry in Figure 15 shows that the path length *l* of the x-ray while it is inside the sample can be written

$$l = \frac{2z}{\sin\theta}. \tag{41}$$

Considering the large number of x-rays that are incident on the sample in XRD analysis and the fact that these x-rays will all penetrate the sample at different points on the surface and

can travel to different depths in the sample, the path length traveled by each will be different. Assuming that scattering probability does not depend on position, the probabilities of all the x-rays can be added together:

$$I = I_0 \int_0^t e^{-2\mu z/\sin\theta}\, dz = I_0\left(1 - e^{-2\mu t/\sin\theta}\right) \tag{42}$$

where t is the thickness of the film. The sum is approximated as an integral due to the large number of x-rays.

Taking the angular dependence of Equation (42) and neglecting the constants, as was done with the polarization constant, gives rise to the attenuation factor:

$$I \propto \left(1 - e^{-\frac{2\mu t}{\sin\theta}}\right). \tag{43}$$

2.3.6. Total Correction Factor

Once these factors have been taken into consideration, Equations (22), (24), (35), (39), and (40) can be combined to find the total angular dependence of the integrated intensity measured from a single grain or orientation:

$$\int I d\theta \propto |F_{hkl}|^2 \frac{(1 + \cos^2(2\theta))}{\sin(2\theta)}\left(1 - e^{-2\mu t/\sin\theta}\right). \tag{44}$$

Continuous theta-2theta scans using an XRD yield data for the intensity of diffracted x-rays with respect to the 2θ angle. Different orientations diffract x-rays at different 2θ angles, as calculated by Bragg's law. In order to determine the percent of each orientation present in a sample from XRD analysis, the effects of orientation on measured intensity need to be isolated. Therefore, dividing out the dependence on the geometry of the instrumentation, the corrected integrated intensity is

$$\left[\int Id\theta\right]_{corrected} = \frac{\int Id\theta}{|F_{hkl}|^2 \frac{(1+\cos^2(2\theta))}{\sin(2\theta)}(1-e^{-2\mu t/\sin\theta})}. \quad (45)$$

When the measured intensity is multiplied by this total correction factor, the remaining effects on angular dependence of integrated intensity are all due to orientation. In this way, texture information can be ascertained from XRD scans.

Chapter 3

XRD APPARATUS

3.1. Overview

The Houghton XRD consists of several components that are contained within a steel case on a tabletop. The x-ray source produces x-rays which are directed through a collimator to the sample located on the sample mount. X-rays are detected by a radiation monitor which transmits this information to a computer. Scans of Bragg angles are facilitated by stepper motors that move the radiation monitor and rotate the sample. A high voltage power supply, along with a battery and several electronic components are housed beneath the table and are used to power the XRD. A computer is also housed under the table to control and run the motors and radiation monitor. An overview of this setup is shown in Figure 16.

1	lead bricks
2	radiation monitor
3	motors
4	sample mount and sample
5	collimator
6	track for motors
7	x-ray source and holder
8	steel shielding
9	acrylic box
10	interlock switches

Figure 16. Overview of Houghton XRD. The sample, detector, and x-ray source are mounted on the table, enclosed in steal case. The electronics and water connection are situated below the table.

3.1.1. Supplying the X-rays

The X-ray source for the Houghton XRD is a Phillips-Norelco x-ray tube, shown in Figure 17, which is powered by a high voltage DC power supply that can reach up to 40 kV. The x-ray tube has a copper target and produces characteristic x-rays that exhibit Cu K-α radiation with a wavelength of 1.5406 Å.

When the XRD is in use, the x-ray tube is housed in a holder shown in Figure 18 that is connected to the high voltage power supply through the circuit shown in Figure 19. The connections in this holder connect the power supply with the filament and the copper target, creating the necessary potential difference to generate x-rays. The holder also has connections for the water-cooling system. These connections are located at the bottom of the x-ray holder which continues through the table and comes out underneath.

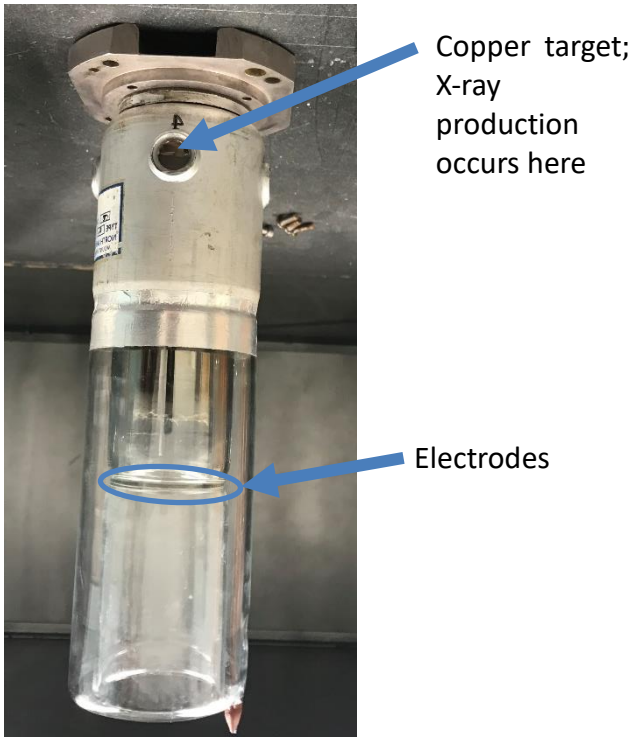

Figure 17. Phillips-Norelco x-ray tube used in Houghton XRD. The copper targets are housed in the metal part at the top of the tube where the production of the x-rays takes place. One target can be seen in the small circle. The electrodes are located in the lower area inside the glass, this is where connections are made with the wires going into the holder.

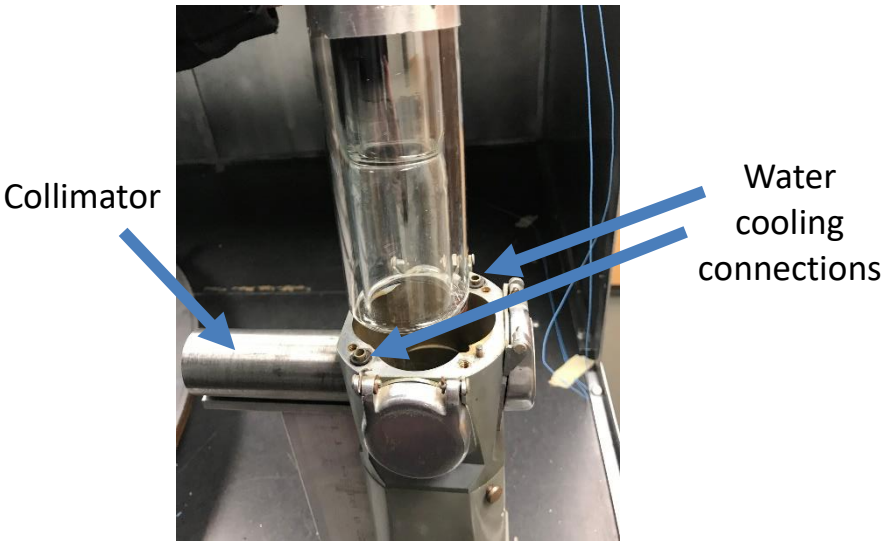

Figure 18. Picture of holder for x-ray tube. The x-ray tube fits in the holder which has the connections for the water-cooling system to reduce the heat generated with the production of x-rays. The x-rays exit the tube and holder through an opening connected to the collimator.

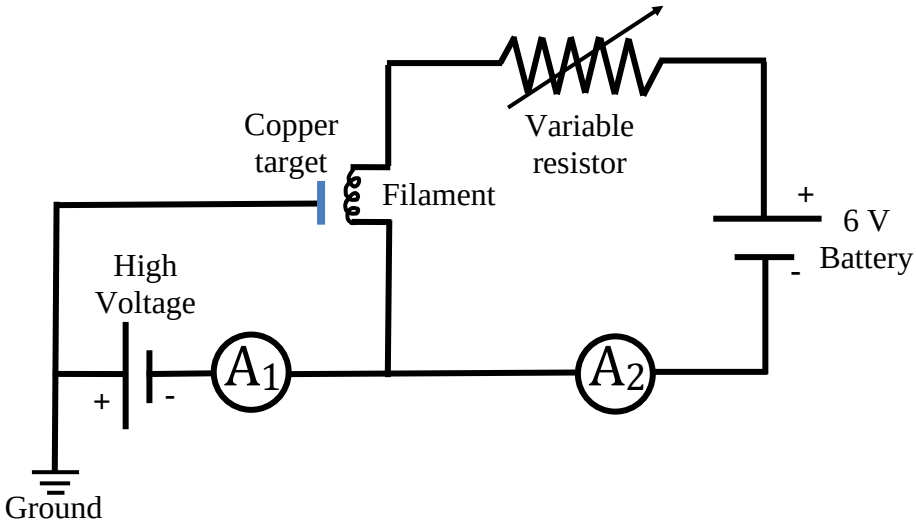

Figure 19. Electronics circuit powering the Houghton XRD. The high voltage power supply floats the filament circuit a high negative voltage (up to -40 kV) while the 6V battery creates a potential difference across the filament. The copper target is connected to ground, this causes electrons to accelerate off of the filament towards the target. Multimeters are included in the circuit to measure current. A_1 measures the beam current which depends on the high voltage supplied while A_2 measures the filament current which is kept around 3 A using the variable resistor.

As the x-rays are produced by the x-ray tube, they leave the holder through an opening in the side of the top that aligns with the copper target in the x-ray tube. They then travel through a 10 cm long collimator with a 0.5 cm inner diameter after which they enter a 64 cm long steel pipe collimator with a 1.5 cm inner diameter as shown in Figure 20. The material of the collimator absorbs x-rays that are not traveling directly towards the sample which reduces the background radiation by eliminating x-rays that would not hit the sample before being detected or would reflect off of another object on the table. Simply put, the collimator ensures that the x-rays travel towards the sample holder.

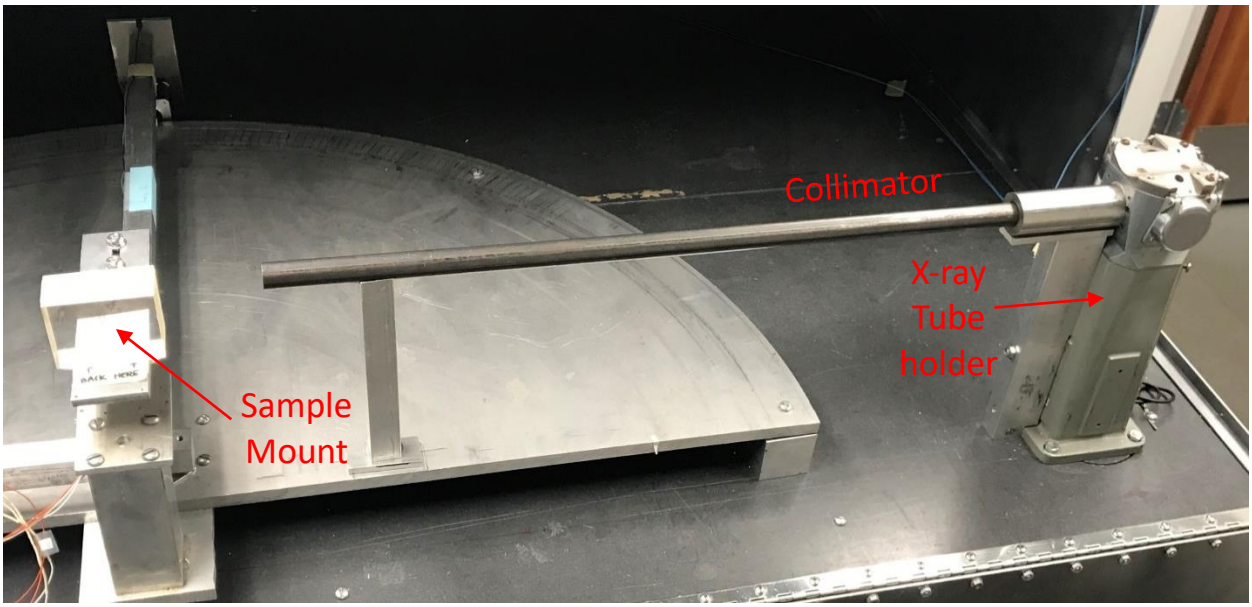

Figure 20. Picture of collimator in table set-up. The short collimator is attached directly to the x-ray tube holder. The longer steel collimator is then attached in sequence. Both collimators are in line with both the x-ray source and the sample mount.

3.1.2. Tabletop Arrangement

The collimator and x-ray source are fixed in position on the tabletop and cannot be moved. This requires that the sample mount and detector can be moved in order for scans to be completed using this equipment. The arrangement of the equipment on the tabletop can be seen in Figure 21.

This equipment includes the x-ray source and collimator as well as a sample mount attached to a long metal arm, a Vernier student radiation monitor attached to a second metal arm, and

a semi-circular track around which two motors move. The sample mount is in line with the x-ray source and collimator, as shown in Figure 20, so that it is in the direct line of the x-rays. The sample mount is a block of plastic material onto which the sample is attached using double-sided tape. The tape ensures that the sample surface is completely open to the x-rays for measurements to take place and that the sample is flat in the plane of the sample mount. The plastic material of the sample mount is important because this plastic does not reflect x-rays with the same angular dependence as is expected from thin film samples under analysis. Due to this, any reflection of the x-rays by the sample mount should only be present in measurements at background levels and will not impact the results of the XRD scans.

The sample mount is mounted on an arm that is attached to a Lin Engineering 101411 stepper motor. The sample mount is firmly attached to the arm which rotates with the motor; this in turn causes the sample mount to rotate with the motor as well. The Vernier student radiation monitor is similarly attached to an arm with a Lin Engineering 101411 stepper motor at the end. As this motor rotates around the semi-circular path the radiation monitor moves around the track to different angles.

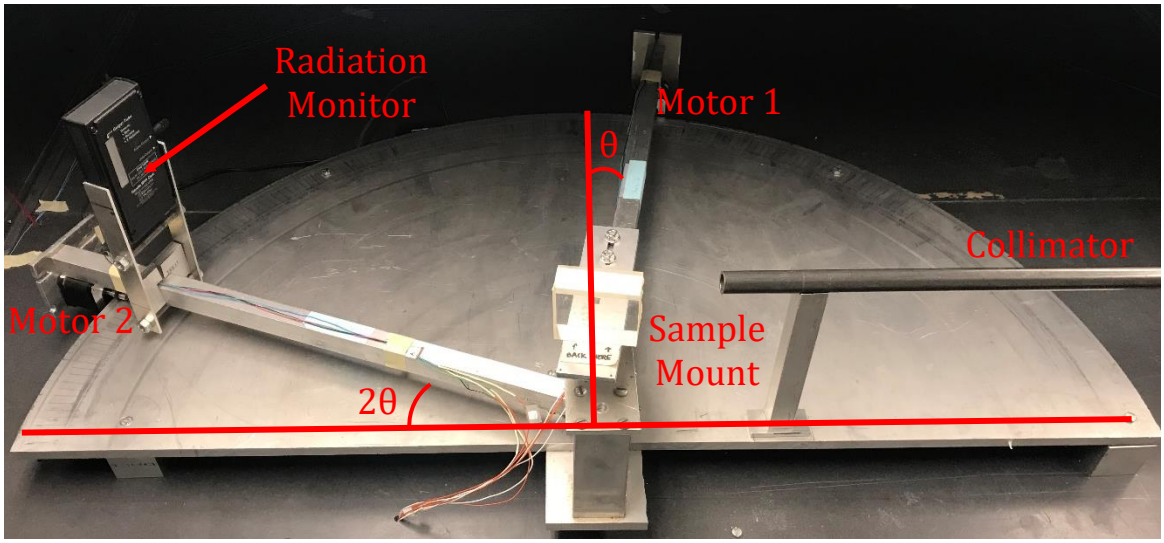

Figure 21. Tabletop arrangement of Houghton XRD. The sample mount is attached to the arm with motor 1 that rotates around the semi-circular track. The radiation monitor is similarly attached to the arm with motor 2 that rotates around the track. As the motors move, the collimator is fixed in place and the entire ensemble preserves the Bragg geometry.

When XRD scans are being performed with this equipment, the x-ray source and collimator remain in a fixed location and a LabVIEW program, which will be explained in Section 3.3.1, controls both motors causing them to move. The movement of the motors, in combination with the stationary x-ray source preserves the geometry necessary for Bragg's Law calculations to be used while also allowing the XRD to scan through a range of Bragg angles.

3.2. Safety Features

When this equipment is in operation, a large number of x-rays are produced. This number has been measured as high as 50370 counts in a 10 second period at 61 cm from the end of the collimator (or 135 cm from the x-ray source). This measurement was taken at approximately 32 kV power from the high voltage with a filament current of approximately 3 A. While the collimator does absorb some of the x-rays generated so that only those travelling towards the sample remain, this still leaves a considerable amount of radiation that must be dealt with. Running the Houghton XRD also involves the use of high voltage which requires extra safety precautions. In order to ensure the safety of the operators, several safety features have been added and updated.

3.2.1. Acrylic Case for Electronics

To address the risk associated with contact with high voltage, the wiring connected to the filament, all of which floats at high voltage and is not grounded, has been placed inside a larger acrylic box. This box, shown in Figure 22, is designed to protect the operators from the high voltage elements used. The equipment in the box includes the 6 V battery, the variable resistor, two multimeters, and the connector that comes directly out of the x-ray tube holder which contains the wires leading to the filament. This box also contains an interlock switch by the door which will be explained in Section 3.2.3.

3.2.2. Dealing with the X-rays

Once the high voltage is running safely, x-rays can be produced. X-rays, as a form of radiation, carry their risks, and while the collimator mentioned above ensure that only x-rays directed towards the sample are free to travel, not all of these will reflect off the sample into the detector. Some may continue to move past the sample mount, without interacting with the

sample surface. To absorb these x-rays, a stack of lead bricks has been placed in line with the collimator and sample mount.

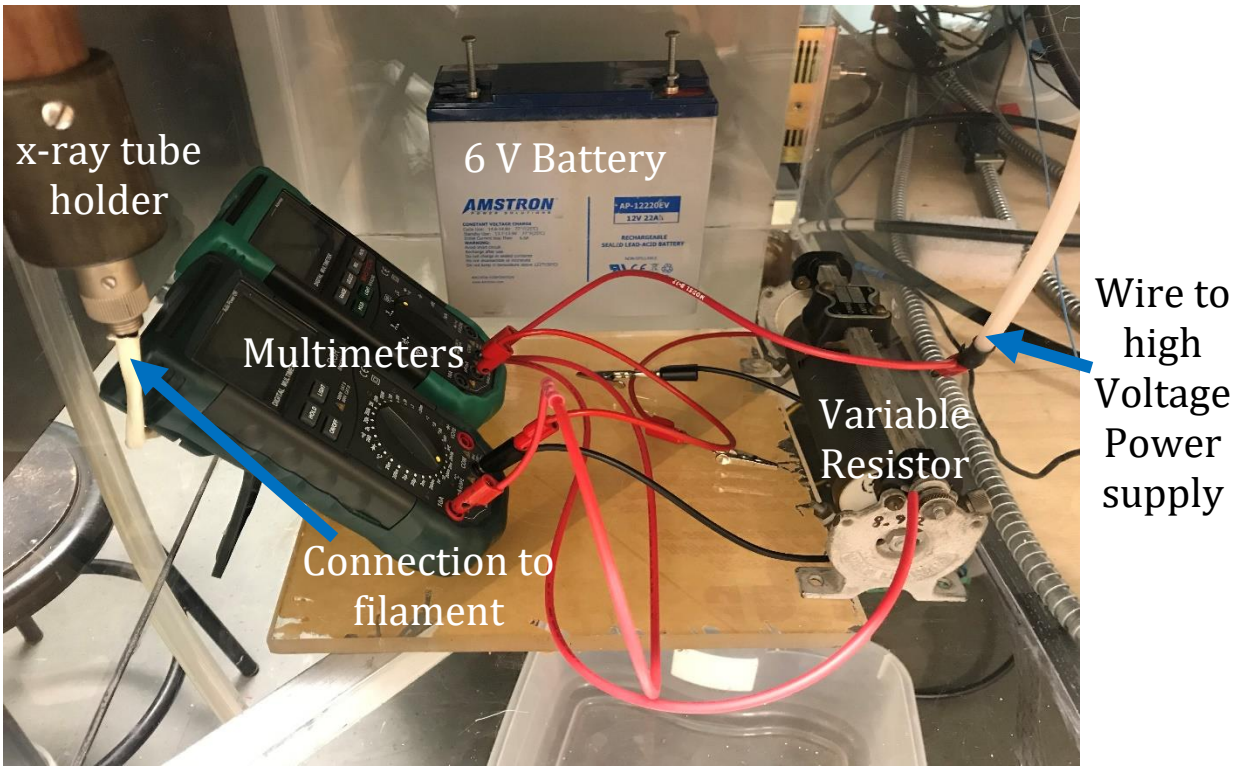

Figure 22. Acrylic box surrounding electronics to contain high voltage circuit. All electronics and connections to electronics that are not grounded are situated within this box.

As an additional safety measure, steel shielding around the entire apparatus has been completed (shown in Figure 23a). Several 0.3175 cm steel panels have been secured around the tabletop to create a box that encloses the XRD equipment. The steel absorbs the radiation that has not been stopped by the lead bricks or directed into the detector. This box has two front panels and two top panels that open, as shown in Figure 23b, allowing access to the equipment. When the XRD is in use, all panels of the shielding are closed and radiation levels in the surrounding room are monitored with a Geiger counter to ensure that radiation stays indistinguishable from naturally occurring background radiation levels. This shielding is important to protect the operators, and any others in the room from levels of radition that have the potential to cause serious and permanent damage to tissue, organs, and other parts of the body.

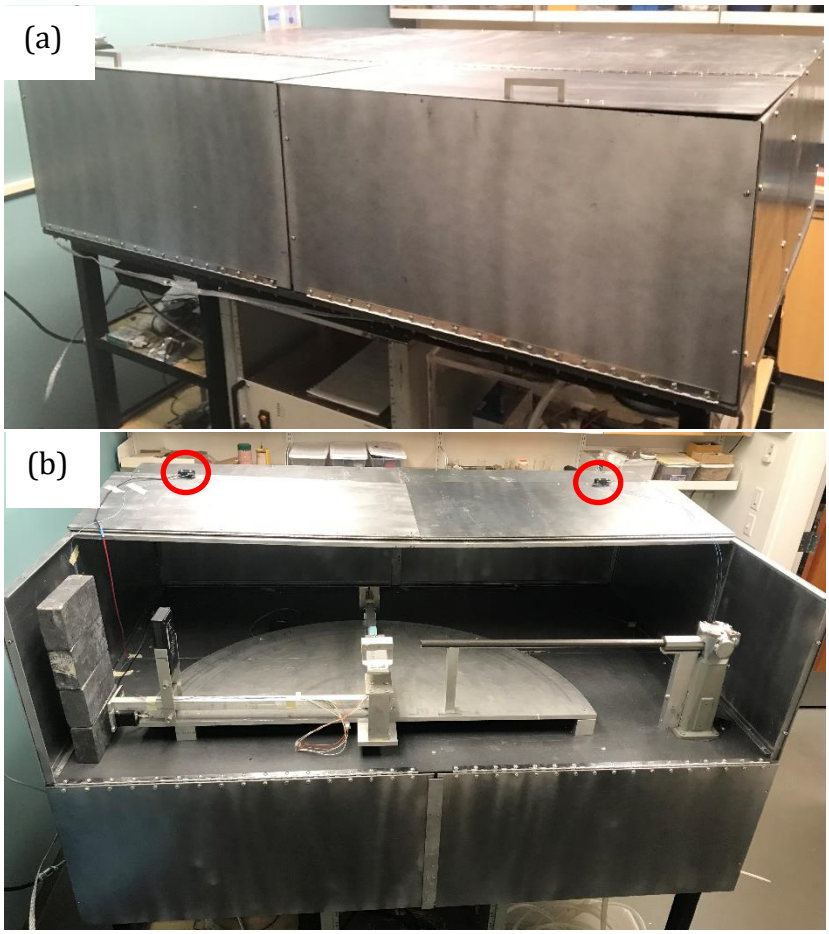

Figure 23. Steel shielding surrounding XRD table. (a) The shielding encloses the entire tabletop to keep radiation out of the room. (b) Two top and two front panels open, allowing access to the equipment for adjustments. The red circles show the interlock switches.

3.2.3. Interlocks

The safety features mentioned thus far can only function effectively when all pieces are in place and all doors closed. To address this, the Houghton XRD has been outfitted with a series of interlocks in an effort to further ensure safety to those in the room while the machine is in use. One interlock is placed on the acrylic box containing the electronics, shown in Figure 22. This switch is closed only when the box is also closed ensuring that power is only supplied to the x-ray source if the door is shut and no one is working on the electronic circuitry that connects to the high voltage power supply.

The panels in the steel shielding that open for access are also outfitted with interlock switches as shown in Figure 23b. These switches are closed only when all panels of the

shielding are shut. This ensures that, if any panel is open through which radiation could escape, the power is shut off and no x-rays can be produced.

3.3. Running the Motors

Another key aspect to running the Houghton XRD is the program that drives the motors, facilitating the desired scans. As stated in Section 3.1.2, computer software controls the stepper motors that move both the sample and the detector. This software sets the acceleration, velocity, and position of the motors. A LabVIEW program has been designed to use this software to create XRD scans with these motors.

3.3.1. MotorStallFIX.vi

The MotorStallFIX.vi program has been developed to carry out continuous θ-2θ scans of samples. This program takes user input for the target 2θ and the degree increments that will be scanned. The input is then converted into the number of times the motors need to move to reach the desired angle using the input angle increment. The angle increment is converted to the proper number of steps for each motor. The block diagram for the program can be found in *Appendix A*.

The degree to step calculation for each motor has been adjusted to address issues with consistency. This conversion has been split into two separate calculations, one for each motor, to ensure that each motor moves the proper number of degrees around the semicircular track. The calibration for each motor was determined experimentally. One-degree angular increments were calculated geometrically, and marks were made on the semicircular track. Adjustments were then made to the current calibration factors until each motor moved consistently to each degree marking with one movement. In this way, calibration factors were determined to be 90.2 steps per degree for the sample motor and 93.7 steps per degree for the detector motor. This empirical calibration was made necessary by the incongruity between the two motors and the deformations that likely occur over time to the rubber o-rings which act as wheels for the motors.

This program also divides the angle increment for each move by two for the sample motor so that the geometry for Bragg's Law is preserved each time the two motors move. This causes the detector motor to move twice as far as the sample motor during each move.

There is also a time delay written into this program that is set by the user and causes the motors to stand still for the desired amount of time before making their next movement. When in use, this allows the detector to measure a greater intensity while it waits at each measurement point.

Chapter 4

CONCLUSION

4.1. Current Status

Although the Houghton XRD has not yet produced data, a considerable amount of progress has been made on the machine.

4.1.1. Physical Components

The basic hardware necessary for scans has been successfully installed in the machine. This includes a functioning x-ray source that is in place with connections to an adequate water-cooling set-up and a high voltage power supply which is connected along with the electronic circuit necessary to power the x-ray source. These components have been tested and successfully produce x-rays.

An adequate radiation monitor is also in place to facilitate data collection and a sample mount has been established to provide a place for samples to be fixed during scans. Other elements including the motors, the arms to which they are attached, and the track around which they move are also in place and have been tested. These elements are now functioning with consistency and the motors now move to the desired/input angle.

The steel shielding and interlocks have also been completed allowing for safe testing of the x-ray components. Similarly, the acrylic box and interlock has also been completed allowing for the high voltage to be run safely.

4.1.2. Software Components

The computer software controlling the motors has been tested as well. The software successfully measures the current location of the motors and the LabVIEW program that has been developed is able to accurately move the motors through a single scan over the desired range of angles.

4.2. Future Plans

Despite all of the components of the Houghton XRD that are functioning as expected, test scans of samples have not yet yielded any peaks in intensity from diffracted x-rays. Several improvements have been suggested to deal with this issue. Some of these address resolution issues that likely contribute to the lack of peaks in the scans. Other improvements are intended address reproducibility issues and to complete the XRD for long-term use.

4.2.1. Improved Resolution

To address the issue of expected low resolution of the current XRD apparatus, a cap has been proposed for the collimator that includes a pinhole, this will narrow the beam of incoming x-rays. A narrower beam will reflect off of the sample in a smaller area and result in fewer interactions between reflected x-rays, which should result in sharper, more noticeable peaks for future scans. Additionally, continued improvements to the sample mount are under consideration in an effort to reduce the number of x-rays reflecting off of the plastic and thereby lower the background radiation detected during scans. The installation of an improved radiation detector is also planned to help increase resolution. In addition, the detector will be covered with a shield leaving only a small hole exposed for x-rays to hit the detector. This should reduce the background noise seen in scans and improve angular resolution.

4.2.2. Improvements for long-term use

Once the XRD is able to produce data, the plan is for it to be put into use full-time for thin film research. This requires that the machine be set up for continuous use over long periods of time. Updates to the water-cooling system are necessary for this. The system is currently run off of a sink when scans are being conducted as they do not last more than an hour or so and the water does not need to be hooked up indefinitely. Plans are in place for the water-cooling system to be permanently hooked up to a water chiller which will allow for scans to be run at any time.

Adjustments to the LabVIEW program controlling the motors will also be made. This is in an effort to have the program reset the motors properly before each scan, allowing it to be used for several consecutive scans without interruption.

4.2.3. Correcting Intensity

Preliminary construction has also begun on adding a second radiation monitor that will measure fluctuations in the intensity of x-rays being produced. This monitor is located in a fixed location near the x-ray source. Using the measurements from this second monitor, fluctuations in intensity of x-rays coming from the source can be divided out from the recorded data. This will allow any peaks that might occur at the low incident intensity to be seen and not drowned out by data that came from a higher incident intensity.

Appendix A

MOTORSTALLFIX.VI BLOCK DIAGRAM

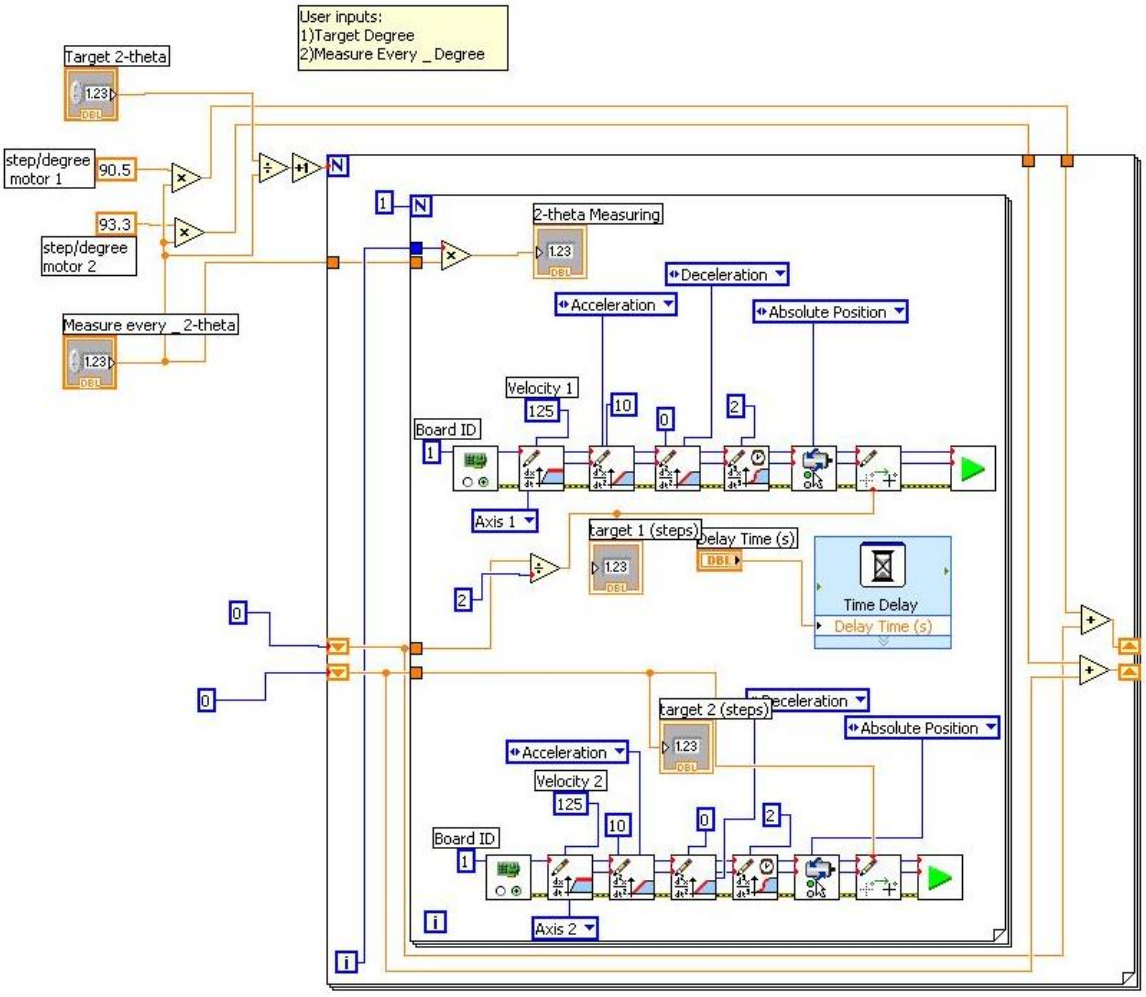

Figure 24. LabVIEW block diagram for MotorStallFIX.vi program used to control the motors and conduct XRD scans. User inputs and the step/degree ratios control the motors to achieve the desired scans. A time delay is also included in the program to facilitate higher intensity measurements during scans.

R e f e r e n c e s

[1] R. R. Babić et. al., Med Pregl **69**, 323 (2016).

[2] W. C. Röntgen, Sitzungberichte der Würzburger Physik-Medic. 1 (1895).

[3] A. S. Ilyushin and M. V. Kovalchuk, Krustallografiya **57**, 693 (2012).

[4] W.H. Bragg, Trans. Roy. Soc. S. Aust. **31**, 79 (1907).

[5] W.H. Bragg, Trans. Roy. Soc. S. Aust. **31**, 94 (1907).

[6] J.J. Thomson, G.P. Thomson, Conduction of Electricity Through Gases, 3rd ed. (Cambridge University Press, London, 1933), Vol.2, Ch. 6, pp. 231, 257-260.

[7] N. Robotti, Red. Fis. Acc. Lincei **24**, 7 (2013).

[8] H. von Helmholtz, Ann. Phys. (Leipzig) **48**, 389 (1893).

[9] A. Sommerfeld, Ann. Phsy. (Leipzig) **38**, 473 (1912).

[10] C.G. Barkla, The London, Edinburgh, and Dublin Phil. Mag. J. Sci. Ser. 6 **22**, 396 (1911).

[11] M. Eckert, Acta Cryst. **A68**, 30 (2012).

[12] C.G. Barkla, Phil. Trans. R. Soc. London, Ser. A **204**, 467 (1905).

[13] W.C. Röntgen, Ann. Phys. **300**, 18 (1897).

[14] H. Haga and C.H. Wind, Ann. Phys. (Leipzig) **68**, 305 (1903).

[15] B. Walter and R. Pohl, Ann. Phys. (Leipzig) **29**, 331 (1909).

[16] W. Friedrich, P. Knipping, M. Laue, Ann. Phys. (Leipzig) **346**, 971 (1913).

[17] W. L. Bragg, Camb. Phil. Soc. Proc. **17**, 43 (1913).

[18] W.L Bragg, Proc. R. Soc. London **89**, 248 (1913).

[19] W.H Bragg, W.L. Bragg, Proc. R. Soc. London **A88**, 428 (1913).

[20] S.P. Baker, B. Hoffman, L. Timain, A. Silvernail, E.A. Ellis, Acta Materialia **61**, 7121 (2013).

[21] P. Sonnweber-Ribic, P. Gruber, G. Dehm, E. Arzt, Acta Materialia **54**, 3863 (2006).

[22] P. Sonnweber-Ribic, P.A. Gruber, G. Dehm, H.P. Strunk, E. Arzt, Acta Materialia **60**, 2397 (2012).

[23] E.A. Ellis, et. al, Acta Materialia **105**, 495 (2016).

[24] A. Sommerfeld, Phys. Z. **10**, 969 (1909).

[25] B.D. Cullity, Elements of X-ray Diffraction (Addison-Wesley, Reading, MA, 1967), pp. 5,8, 105.

[26] International Tables for X-ray Crystallography edited by Caroline H. MacGillavry and Gerard D. Rieck (Kynoch Press, Birmingham, England, 1968) Vol III, pp 202-207.
[27] M.J. Buerger, Proc. Natl. Acad. Sci. U.S.A. **26**, 637 (1940).